Development and validation of a clinical decision support system based on PSA, microRNAs, and MRI for the detection of prostate cancer

International Journal of Hydrogen Energy 140 (2025) 119–130

Contents lists available at ScienceDirect

International Journal of Hydrogen Energy

journal homepage: www.elsevier.com/locate/he

Progress in the study of glass-based systems as sealants for proton ceramic electrolysis cell assembly

Francesco Da Prato [a,*], Simone Anelli [b], Andrea Moranti [a], Domenico Ferrero [a], Massimo Santarelli [a], Federico Smeacetto [b]

[a] Department of Energy (DENERG), Politecnico di Torino, 10129, Turin, Italy
[b] Department of Applied Science and Technology (DISAT), Politecnico di Torino, 10129, Turin, Italy

ARTICLE INFO

Handling Editor: Fanglin F. Chen

Keywords:
Proton ceramic cells
Glass-sealant
Glass composite
Single repeating unit
Hydrogen production

ABSTRACT

This study compares a commercial boron-based glass and its composite, obtained by adding 5 wt% 3YSZ, with a silica-based glass as sealants for joining AISI 441 ferritic stainless-steel interconnectors to BZCY622/NiO-BZCY622 protonic ceramic half-cells. The boron-based glass and its composite exhibited lower glass transition temperatures (500°C–600 °C), making them well-suited for the operating range of PCECs. The composite approach enabled tuning of the viscous flow behavior, softening temperature, and coefficient of thermal expansion (CTE) while also enhancing the thermal stability. SEM-EDX characterization of samples joined with the composite system confirmed no significant structural evolution after aging for 500 h at 600 °C in an air-steam mixture (70 %–30 % vol.). Both the boron-based glass and its composite effectively relaxed stresses induced by CTE mismatch between the joined layers and by the chemical expansion of the electrolyte, demonstrating excellent thermal stability under severe cycling conditions in an air-steam mixture (70 %–30 % vol.).

1. Introduction

In recent decades, the significant increase in global energy demand and the resulting rise in CO_2 emissions have underscored the urgent need for sustainable energy solutions. While renewable energy sources are essential in addressing this challenge, their intermittent nature necessitates the integration of efficient energy storage technologies [1,2]. The power-to-hydrogen strategy, which involves converting excess electricity into storable hydrogen via steam electrolysis, is an efficient and economically viable option [3]. Hydrogen enables long-term energy storage and serves as a clean fuel and feedstock for industrial processes [4]. As a result, electrolyzers have become a focal point of research and development, aiming to enhance efficiency, durability, and cost-effectiveness [5]. High-temperature electrochemical cells, such as solid oxide electrolysis cells (SOECs) and proton ceramic electrolysis cells (PCECs), show promise for power-to-X electrolyzer technologies, offering thermodynamic and kinetic advantages that enable high efficiency [6]. Unlike SOECs, which transport oxygen ions (O^{2-}) from the fuel to the oxygen electrode through the electrolyte, PCECs operate by conducting protons (H^+). This proton conduction mechanism results in lower activation energy, due to the smaller ionic radius of H^+ compared to O^{2-} [7], and enables high efficiency within the intermediate temperature range (400–600 °C) [8]. As a result, the materials used in PCECs experience reduced thermal degradation relative to SOECs, which typically operate at higher temperatures (700–1000 °C), thereby improving long-term durability [9]. Additionally, in PCECs, water vapor is directly supplied to the oxygen electrode side, enabling the production of pure hydrogen at the fuel electrode side without dilution. This configuration eliminates the need for downstream hydrogen separation processes, thereby reducing system costs and enhancing overall economic viability [8].

Regarding the SoA materials for PCECs, single-phase ABO_3 perovskites with the composition $Ba(Ce, Zr)O_{3-\delta}$ (BCZY), doped with rare earth elements such as Y or Yb, are among the most widely used electrolytes, exhibiting excellent chemical stability and high proton conductivity [10,11]. The high proton conductivity of these perovskites is attributed to the partial substitution of tetravalent cation (Zr^{4+} or Ce^{4+}) at the B-site with a trivalent cation, such as Y^{3+} or Yb^{3+}, which promotes the formation of oxygen vacancies. During the hydration process, water vapor dissociates and incorporates into the ceramic lattice, filling the oxygen vacancies and forming hydroxyl defects (OH^+), through which H^+ are subsequently conducted [12]. The fuel electrode must exhibit

* Corresponding author.
E-mail address: francesco.daprato@polito.it (F. Da Prato).

https://doi.org/10.1016/j.ijhydene.2025.05.286
Received 15 March 2025; Received in revised form 14 May 2025; Accepted 20 May 2025
Available online 29 May 2025

sufficient electronic and ionic conductivity, as well as catalytic activity for hydrogen oxidation and evolution reactions. Ni-based cermet, composed of Ni and a proton-conducting phase like BCZY, are the most commonly used materials [13]. The oxygen electrode must provide active sites for electrochemical reactions, including oxygen reduction, oxygen evolution, and water splitting while maintaining sufficient electronic conductivity for efficient current collection [14]. Mixed ionic and electronic conductors (MIECs), such as $Ba_{1-x}Sr_xCo_{1-y}Fe_yO_{3-\delta}$ (BSCF) and $La_{1-x}Sr_xCo_{1-y}Fe_yO_{3-\delta}$ (LSCF), are among the most commonly used materials for the oxygen electrodes.

However, similar to SOECs, a single PCEC exhibits a low hydrogen production rate. For example, a current density of -1.92 A cm^{-2} at 600 °C and 1.3 V with an estimated Faradaic efficiency of 76 % was reported [15]. This corresponds to a hydrogen production rate of approximately 11 Nml/min for a single cell [8]. The cells measured in the mentioned study are composed of $PrBa_{0.5}Sr_{0.5}Co_{1.5}Fe_{0.5}O_{5+\delta}$ (PBSCF) double perovskite as the air electrode, $BaCe_{0.4}Zr_{0.4}Y_{0.1}Yb_{0.1}O_{3-\delta}$ (BCZYYb) as the electrolyte, and NiO-BCZYYb as the fuel electrode—materials considered among the state of the art in terms of performance [9]. To increase the final hydrogen output, several cells must be assembled into single repeating units (SRUs), which are then combined in series to form a stack [16,17]. In a classical planar configuration, the SRU consists of a complete cell, comprising an oxygen electrode-electrolyte–fuel electrode structure, joined with a properly designed sealant to the interconnect. The interconnect serves as the functional element that provides structural stability to the SRU while establishing the electrical connection between the oxygen electrode of one cell and the fuel electrode of the adjacent one [18]. Ferritic stainless steels (FSSs) are the most promising materials for metallic interconnects [19]. For instance, AISI 441, AISI 430, Crofer 22 APU, and Crofer 22H [20–22] have demonstrated effectiveness as interconnects and frames due to their excellent corrosion resistance and compatible CTE with the other elements of the PCEC SRUs. Their CTE values, typically in the range of 11–12 $\times$ 10^{-6} K^{-1} [23,24], are well-matched with the CTEs of doped BCZY perovskites, which range from 8–13 $\times$ 10^{-6} K^{-1} [25]. The sealant is the functional element that joins the cell to the interconnect, ensuring gas tightness, electrical insulation, and chemical and mechanical stability between the different coupled materials. Drawing from experience with SOCs [26–28], glass and glass-ceramic sealants have emerged as the most effective solutions for meeting these requirements. Their thermomechanical properties, including glass transition temperature (T_g), softening temperature (T_s), CTE, and chemical and thermal stability, can be optimized by carefully fine-tuning their compositions, making them versatile and adaptable to the different operating conditions of the specific application [29]. For optimal performance, the seal glass should have a T_g slightly below the stack's operating temperature (~600 °C) to allow viscous flow for self-healing cracks while maintaining sufficient rigidity. The T_s should be 30–40 °C higher than the operating temperature to prevent excessive flow [29]. CTE mismatches between joined materials should be maintained below 1–1.5 $\times$ 10^{-6} K^{-1}. At the same time, the sealant must demonstrate long-term chemical and thermal stability under strongly oxidizing and steam-rich conditions at the oxygen electrode side, and reducing conditions at the fuel electrode side [30]. Glass-ceramic systems designed for SOFCs/SOECs generally exhibit T_g and T_s values that are too high for the target operating temperatures of PCECs. As demonstrated in a previous study [22], where three glass systems designed for SOFCs/SOECs applications were tested for joining BCZY721 electrolytes to FSS AISI 441, the high joining temperatures of these systems led to instability phenomena in the electrolyte itself (e.g., Ba-depletion) at the interface with the glass. In addition to thermal stresses from CTE mismatches, PCECs experience unique mechanical challenges due to the chemical expansion of the electrolyte [31]. Chemical expansion occurs during the hydration reaction of BZCY perovskite, where water is absorbed into the crystal lattice, forming protonic defects [7]. This process, which occurs in humidified conditions between 300 and 500 °C depending on the steam partial pressure (pH_2O), induces lattice distortions that generate additional tensile stresses within the cell [25,32,33]. Chemical expansion is particularly critical during PCEC stack startup or when temperature fluctuations deviate from the operating temperature, further exacerbating mismatches between individual material components in the electrochemical device. Being able to relax these combined mechanical stresses is therefore crucial for the sealant to ensure the durability and reliable performance of PCEC systems [34]. Only a few studies have been published on designing and characterizing glass-based sealants for PCEC integration. A SiO_2–TiO_2–K_2O–Na_2O–Al_2O_3–ZnO glass sealant was developed and used to join Mn–Co coated Crofer22H to $BaZr_{0.2}Ce_{0.7}Y_{0.1}Yb_{0.1}O_{3-\delta}$ (BZCYYb) electrolyte, demonstrating mechanical and thermal stability even after ageing in a humid oxidizing atmosphere at 600 °C for 300 h [21,35,36].

In this study, a commercial boron-based glass rich in Ba and Ca was investigated as a potential glass sealant to join FSS AISI 441 to $BaZr_{0.625}Ce_{0.2}Y_{0.175}$ (BZCY622)/NiO-BZCY622 (60:40 wt%) half-cells. For comparison, a silica-based glass, already studied for SOECs and PCECs [22], was tested with BZCY622 and compared to the boron-based glass. Thermal analyses revealed that the boron-based glass exhibits a lower T_g and T_s than silica-based glass, making it more suitable for the lower operating temperature range of PCECs [30]. Its higher B_2O_3/SiO_2 ratio stabilizes its amorphous phase and improves wettability with BZCY622 [37]. Additionally, the lower joining temperature of the boron-based glass (700 °C vs. 850 °C for silica-based glass) enhanced the stability of the BZCY622 interface. However, its low viscosity at 700 °C (~$10^{4.5}$ P) could cause sealant squeezing during assembly. To address this issue, glass-composite systems were developed by dispersing microfine 3YSZ powder into the boron-based glass. The addition of 3YSZ filler has been shown to effectively hinder the viscous flow behavior of glass and improve its mechanical properties. [38,39]. Boron-based glasses generally exhibit low chemical and thermal stability, leading to significant volatilization of boron species such as $B(OH)_3$ and HBO_2 under high-temperature (700–1000 °C), steam-rich conditions [40]. This volatilization can result in pore formation and weaken the mechanical integrity of the sealant. X-ray diffraction (XRD) analyses showed that optimizing the 3YSZ content promoted controlled crystallization, forming calcium and barium borates already during the joining process. This induced crystallization, combined with the low vapor pressure of volatile boron species at PCEC operating temperatures (500–600 °C), appeared to suppress boron volatilization. Post-mortem characterization using scanning electron microscopy with energy-dispersive X-ray spectroscopy (SEM-EDX) revealed significant structural evolution of the boron-based glass after 500 h of thermal ageing at 600 °C in air-steam mixture (70 %–30 % vol.). In contrast, the boron-based composite glass maintained its structural integrity under the same conditions, demonstrating improved thermal stability. The composite approach enhanced the chemical and thermomechanical stability of the sealant, making it suitable for long-term use in PCEC stacks. Finally, a thermal cycle test between 25 °C and 600 °C with a 2-h dwell time in an air-steam mixture (70 %–30 % vol.) demonstrated that both boron-based and boron-based composite glasses withstood the stresses induced by CTE mismatches and the chemical expansion of the BZCY622 perovskite. In summary, the innovative aspect of this study lies in the development of a composite glass sealant tailored for PCEC applications. It combines the benefits of boron-rich glasses—such as low joining temperature, good wettability, and stress relaxation—with the addition of 3YSZ, which improves viscosity control, promotes crystallization, and enhances thermal and chemical stability by reducing boron volatilization. This approach offers a reliable solution for long-term PCEC integration.

2. Experimental

2.1. Glass sealants selection, preparation and characterization

The first system is a silica-based glass selected for its excellent compatibility with AISI 441 substrates and its promising compatibility with PCECs. The silica-based glass, labeled V11, was designed at the Politecnico di Torino, with its composition detailed elsewhere [41]. It was prepared by weighing and mixing high-purity precursors (oxides and carbonates, Sigma-Aldrich, purity >99.99 %). The resulting homogeneous powder mixture was heated at 1600 °C for 30 min with a lid, followed by 30 min without a lid, in a chamber furnace (Nabertherm GmbH, Germany) under ambient air using a Pt–Rh crucible. The molten glass was then quenched in deionized water. The resulting glass was milled using zirconia balls (Fritsch Pulverisette 5, Mark Einersheim, Germany) and sieved to a particle size <25 μm. The second system is a commercial boron-based glass with lower characteristic temperatures. This commercial glass, GM31107, is produced by SCHOTT AG (Landshut, Germany), and has a declared particle size distribution $D_{50} = 3$ μm. Its composition is presented in Table 1.

2.2. Glass composite sealants formulation and characterization

To improve the softening temperature, viscosity, and wettability of the GM31107 glass on the BZCY622 substrate at the joining temperature, microfine 3YSZ powders (Sigma-Aldrich, Germany) with a declared $D_{50} = 0.7$ μm were incorporated as additives in three different weight fractions: 2.5 %, 5 %, and 10 % (relative to the total weight of the GM31107 powders). The resulting composite systems were labeled GM31107+3YSZ 2.5 %, GM31107+3YSZ 5 %, and GM31107+3YSZ 10 %. These composite systems were prepared by formulating organic pastes with a solid loading of 75 wt%. GM31107 glass powders and the respective 3YSZ fractions (2.5 wt%, 5 wt%, and 10 wt%) were dispersed in propylene glycol (Sigma-Aldrich) as the organic solvent. Polyvinylpyrrolidone K90 (Sigma-Aldrich, Germany) was used as a binder at 1 wt% relative to the liquid fraction, while polyvinylpyrrolidone K30 (Sigma- Aldrich, Germany) was added as a dispersant at 1 wt% relative to the solid content. The mixtures were homogenized using a planetary mixer (THINKYMIXER ARE-250 CE, Japan), with alternating mixing and defoaming steps for 5 min at 1600 rpm. All glass powders (V11 and GM31107) and composite glass powders (GM31107+3YSZ 2.5 %, GM31107+3YSZ 5 %, and GM31107+3YSZ 10 %) were characterized by differential scanning calorimetry (DSC 404 F3 Pegasus, Netzsch, Germany) to study their glass transition and crystallization behavior. The analysis was conducted under a flow of 50 ml/min of air and 20 ml/min of argon (as protective gas). Approximately 20 mg of glass was placed in a Pt crucible and subjected to thermal treatment at a heating rate of 5 °C/min from room temperature to 1200 °C. Thermal characterization was also performed using hot-stage microscopy (HSM, Hesse Heating Microscope, Germany) on the same set of samples. For the composite systems, the previously prepared pastes were dried in an oven (Heraeus T6060 oven) at 90 °C for 20 min, then milled with zirconia ball (Fritsch, Pulverisette 5, Mark Einersheim, Germany) and sieved to obtain particle sizes below 25 μm. Cylindrical samples (2 mm in diameter and 2 mm in height) were pressed from the powders and placed on fragments of BZCY622/NiO-BZCY622 half-cells. These samples were heated in static air from room temperature to the melting temperature, as determined by the instrument. A digital camera recorded the morphological changes of the pellets during heating, providing insights into the sintering behavior, viscous flow behavior, and wettability of the glasses and composite glass systems.

Table 1
Composition in wt% of GM31107 glass.

Element	Al_2O_3	B_2O_3	BaO	CaO	SiO_2
wt.%	10–50	10–50	>50	1–10	1–10

2.3. Joining, aging and cycling thermal treatment and post mortem characterization

Based on the thermal analysis results (Section 3.1), the GM31107+3YSZ 5 % composite system, GM31107 and V11 were selected to fabricate dummy samples in an FSS/sealant/half-cell sandwich configuration for thermochemical compatibility testing. Half-cell fragments, composed of BZCY622/NiO-BZCY622 (provided by Forschungszentrum Jülich) were paired with square pieces of AISI 441 stainless steel (1 cm × 1 cm × 0.3 mm) supplied by Aperam Stainless Service and Solutions Italy Srl. Organic pastes for each system were prepared as described before and applied to the AISI 441 pieces for joining with the half-cells. Thermal treatments were conducted in static air using a Nabertherm 1300 furnace (GmbH, Germany). V11 samples were treated at 850 °C for 1 h, while GM31107 and GM31107+3YSZ 5 % were treated at 700 °C for 30 min. A heating and cooling rate of 5 °C/min was applied for all systems.

To further evaluate chemical and thermal compatibility, the joined samples underwent thermal ageing at 600 °C for 500 h in an air-steam mixture (70 %–30 % vol.). Additionally, thermal cycling from 25 °C to 600 °C was performed for six cycles in the same atmosphere to assess mechanical stability under thermal and chemical stresses caused by CTE mismatches and chemical expansion of BZCY622 perovskite. These tests were conducted in a muffle furnace (ECN, Netherlands).

Cross-sections of the joined samples were analyzed before and after aging and thermal cycling using SEM-EDX analysis. A field-emission SEM (FE-SEM, MIRA3 XMH TESCAN) equipped with an EDS detector was used to examine the morphology and composition of the joining layers. Samples were embedded in epoxy resin (Struers, Denmark), polished with SiC abrasive papers of varying grit sizes (Hermes Schleifmittel GmbH), and sputtered with a thin platinum layer (ZEISS, Germany) to enhance conductivity.

The CTEs of the glasses and composite systems were evaluated after the corresponding thermal treatment and subsequent thermal ageing using a dilatometer (DIL402PC, Netzsch, Germany). After joining and ageing, XRD analyses were performed on the selected glasses and composite powders using an X-Pert Pro MRD diffractometer (Philips, Almelo, The Netherlands). Phase identification was conducted using X-Pert HighScore software (Malvern Panalytical, United Kingdom) and JCPDS reference files.

3. Results and discussion

3.1. Glass characterization

The boron-based (GM31107) and the silica-based (V11) systems have different primary glass network formers, resulting in distinct characteristic temperatures. Fig. 1 presents the HSM and DSC plots of the two selected glasses. The DSC analysis (dashed lines in Fig. 1) revealed an onset of crystallization at 800 °C and a crystallization peak at 845 °C for V11. In contrast, no crystallization peaks were observed for GM31107, demonstrating that its amorphous nature was mostly preserved even at higher temperatures during the thermal treatment. The T_g was identified as the onset of the first endothermic transition (decreasing step) and was found to be 625 °C for V11 and 540 °C for GM31107.

For a sealant, having the T_g within the operational temperature range of the target application promotes viscous flow of the glass, facilitating self-healing of microcracks caused by thermal expansion mismatch between adjoining components during thermal cycling. The T_g of V11 exceeds the PCEC operating temperature range (500–600 °C), while the T_g of GM31107 falls within this range, making it better suited for self-healing under operational conditions. From the HSM analyses (solid line in Fig. 1) performed on the surface of BZCY622 substrates, 1) first

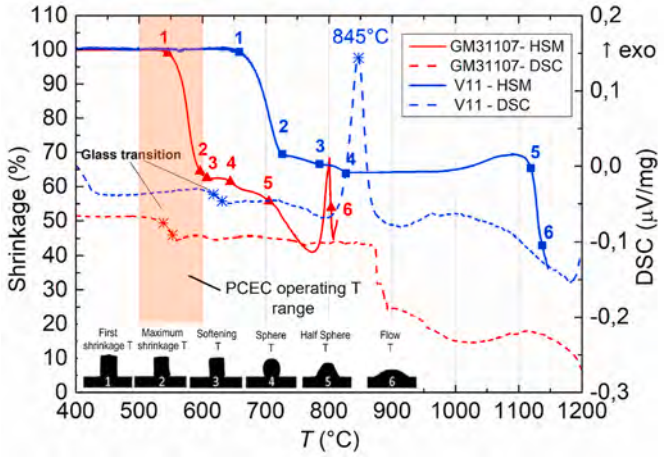

Fig. 1. HSM and DSC curves for the GM31107 and V11 glass systems. Asterisks on the DSC curves mark the glass transition temperature (T_g) and crystallization peak temperature (T_x) for the analyzed glass systems. Red triangles and numbered blue squares on the HSM curves represent the characteristic temperatures identified for GM31107 and V11, respectively. The inset displays digital images corresponding to these characteristic temperatures. The light orange rectangle highlights the operating temperature range of PCECs. (For interpretation of the references to color in this figure legend, the reader is referred to the Web version of this article.)

shrinkage temperature (T_{fs}), 2) maximum shrinkage temperature (T_{ms}), 3) softening temperature (T_s), 4) sphere temperature (T_b), 5) half-sphere temperature (T_{hb}), and 6) flowing temperature (T_m) can be determined. Table 2 summarizes the characteristic temperatures of the two glass systems.

By combining the results of the DSC and HSM analyses, a joining temperature of 850 °C, previously selected for the V11 system, is confirmed. The crystallization peak identified by DSC analysis at T_x = 845 °C is higher than the maximum shrinkage temperature T_{ms} = 726 °C, indicating no overlap between the crystallization and sintering processes. Consequently, crystallization does not compromise the final density of the V11 glass. The maximum shrinkage of the V11 glass is approximately 35 %, stabilizing and reaching a plateau between 700 °C and 800 °C. The T_s was measured at 785 °C.

In contrast, GM31107 exhibits lower characteristic temperatures. The DSC and HSM results confirm the manufacturer's recommended joining temperature of 700 °C. The maximum shrinkage of GM31107, approximately 40 %, is higher than that of V11 and stabilizes within a narrower temperature range of 600–650 °C. Beyond this range, the glass begins to flow, further increasing its shrinkage. A swelling of approximately 30 % is detected between 780 °C and 800 °C. The T_s was measured at 607 °C. According to previous findings [42], the lower T_g and T_s values in glass systems like GM31107 are attributed to its B_2O_3 content. This increases the concentration of non-bridging oxygen--containing silicate structural units and trigonal boroxyl groups, inducing structural changes that reduce the connectivity of the glass network.

To optimize the composite formulation, HSM analyses were performed on the composite systems GM31107+3YSZ 2.5 %, GM31107+3YSZ 5 %, and GM31107+3YSZ 10 %. Fig. 2a presents the results of these analyses.

Table 2
Characteristic temperatures of V11 and GM31107 obtained by HSM.

Glass systems	V11	GM31107
T_{fs} (°C)	658	545
T_{ms} (°C)	726	596
T_s (°C)	785	607
T_b (°C)	827	644
T_{hb} (°C)	1119	705
T_f (°C)	1137	803

As shown in Table 3, dispersing 3YSZ within the glass generally raises the characteristic temperatures of the composite. Specifically, the T_s of GM31107+3YSZ 5 % and GM31107+3YSZ 10 % increases to 641 °C and 649 °C, respectively. Furthermore, the maximum shrinkage for both GM31107+3YSZ 5 % and GM31107+3YSZ 10 % is approximately 35 %, stabilizing between 600 °C and 800 °C. This behavior arises because the rigid 3YSZ inclusions hinder the flow of the glassy matrix, thereby increasing its viscosity [43]. Fig. 2b illustrates the viscosity curves determined using the VFT model [44,45], showing that the viscosity of the composite increases with the mass fraction of 3YSZ, with the effect being more pronounced for GM31107+3YSZ 10 %. Dispersing 3YSZ into the GM31107 at 5 % and 10 % allows fine-tuning of the composite's characteristic temperatures. This ensures that T_g remains slightly below the target operating range, while T_s increases by 40–50 °C above the target range of 550–600 °C. The increased viscosity minimizes excessive viscous flow, reducing the risk of sealant squeezing out during the thermal joining process.

Fig. 3 shows the XRD patterns of the GM31107 powders and its composites after the joining thermal treatment at 700 °C. For GM31107, which remains predominantly amorphous, small peaks corresponding to the β-BaB_2O_4 phase (#PDF 00-024-0086) were detected, consistent with previous findings in barium borosilicate glasses [46]. For GM31107+3YSZ 2.5 %, peaks associated with 3YSZ (#PDF 01-083-0113) and β–BaB_2O_4 (#PDF 00-024-0086) were observed. For GM31107+3YSZ 5 % in addition to 3YSZ (#PDF 01-083-0113), peaks for the new crystalline phase $Ca_5Ba_2B_{10}O_{22}$ (#PDF 00-051-0330) were identified. This phase was previously reported [47] in a BaO–CaO–Al_2O_3–B_2O_3 –SiO_2 glass system. For GM31107+3YSZ 10 %, dominant peaks correspond to 3YSZ (#PDF 01-083-0113) and $CaZrO_3$ (#PDF 01-075-0358), which forms due to the reaction between 3YSZ and glass elements [48]. Previous work reported the XRD pattern of V11 after the joining thermal treatment at 850 °C [22].

Fig. 4 presents the DSC analyses of GM31107, GM31107 + 3YSZ 2.5 %, GM31107 + 3YSZ 5 %, and GM31107 + 3YSZ 10 % glass systems. Again, no crystallization peak is observed in the DSC curve of the unmodified GM31107 glass, consistent with XRD results confirming its fully amorphous nature after the DSC heat treatment. Similarly, no clear crystallization peak is detected for the GM31107 + 3YSZ 2.5 % composite; however, XRD analysis reveals the onset of slight crystallization. This indicates that the crystalline fraction is minimal and likely develops gradually over a broad temperature range, resulting in a weak and diffuse exothermic signal that remains below the DSC detection threshold. In contrast, the GM31107 + 3YSZ 5 % and 10 % composites display distinct crystallization behavior, with onset temperatures (T_{on}) of approximately 740 °C and 730 °C, and crystallization peak temperatures around 760 °C for both systems. Notably, the 10 % composite shows an earlier onset and a more intense exothermic peak, suggesting a stronger nucleating effect due to the higher YSZ content and a greater extent of crystallization. Despite the higher onset and peak temperatures observed in DSC, XRD analysis confirms that partial crystallization occurs in the 2.5 %, 5 %, and 10 % composites after the joining thermal treatment at 700 °C for 30 min. This behavior can be attributed to the extended dwell time and the nucleation-promoting effect of YSZ, which together enable substantial crystallization even at temperatures below those detected by DSC.

The CTE of V11 after the joining thermal treatment at 850 °C was ≈11.67 × 10^{-6} K^{-1} in the 200–500 °C range. The CTE values for GM31107, GM31107+3YSZ 2.5 %, GM31107+3YSZ 5 %, and GM31107+3YSZ 10 % in the 200–500 °C range after the joining thermal treatment at 700 °C were ≈11.4 × 10^{-6} K^{-1}, ≈11.1 × 10^{-6} K^{-1}, ≈10.9 × 10^{-6} K^{-1}, and 10.6 × 10^{-6} K^{-1}, respectively. The decrease in the CTE with increasing 3YSZ content reflects the lower CTE of 3YSZ (10.3 × 10^{-6} K^{-1} in the 200–500 °C range) [43,49], consistent with the rule of mixtures. Additionally, the formation of crystalline phases identified in Fig. 3 may also affect CTE. For the anisotropic crystal phase β– BaB_2O_4,

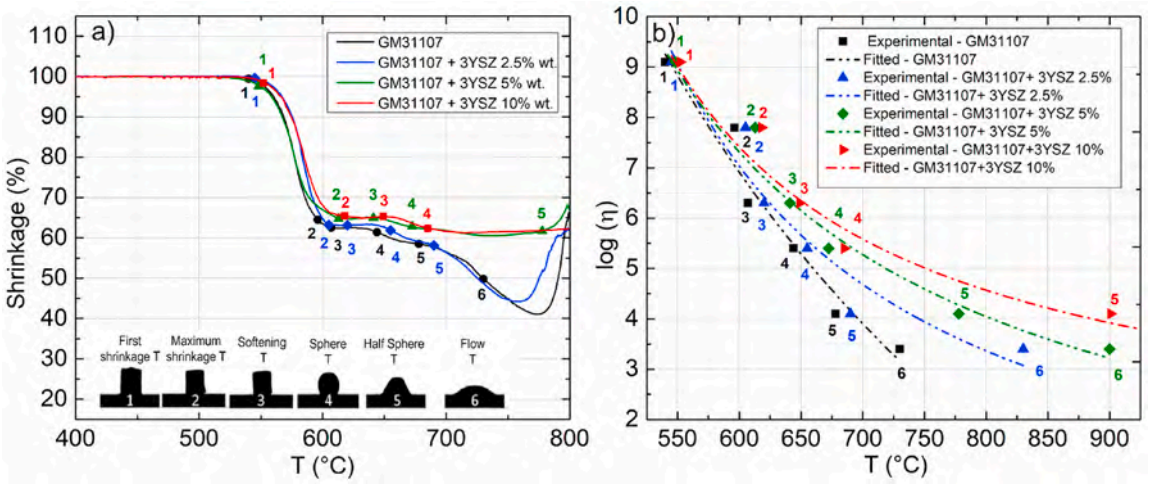

Fig. 2. HSM curves of the GM31107 composite systems (a). The black circles, blue diamonds, green triangles, and red squares represent the characteristic temperatures for GM31107, GM31107 + 3YSZ 2.5 %, GM31107 + 3YSZ 5 %, and GM31107 + 3YSZ (10 %), respectively. The inset displays digital images corresponding to these characteristic temperatures. Viscosity curves were obtained with the VFT model from the HSM curves (b). Again, the black circles, blue diamonds, green triangles, and red squares represent the characteristic temperatures for GM31107, GM31107 + 3YSZ 2.5 %, GM31107 + 3YSZ 5 %, and GM31107 + 3YSZ 10 %, respectively. (For interpretation of the references to color in this figure legend, the reader is referred to the Web version of this article.)

Table 3
Characteristic temperatures of GM31107, GM31107 2.5 %, GM31107 5 % and GM31107 10 % obtained by HSM.

Glass systems	GM31107	GM31107+3YSZ 2.5 %	GM31107+3YSZ 5 %	GM31107+3YSZ 10 %
T_{fs} (°C)	540	545	548	552
T_{ms} (°C)	596	605	613	618
T_s (°C)	607	620	641	649
T_b (°C)	644	655	672	685
T_{hb} (°C)	678	690	778	901
T_f (°C)	730	830	900	1010

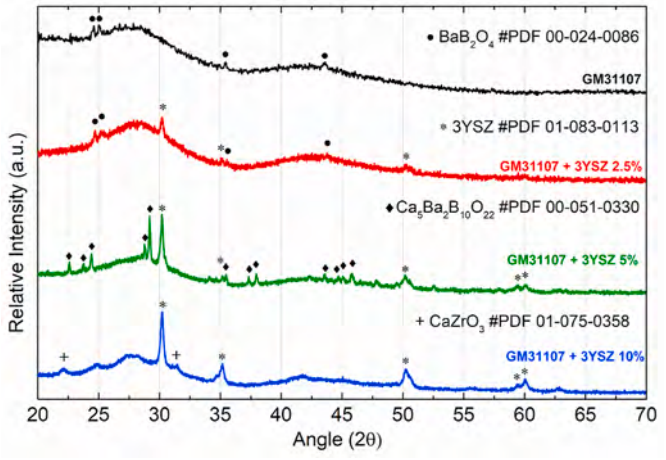

Fig. 3. XRD pattern of the GM31107, GM31107+3YSZ 2.5 %, GM31107+3YSZ 5 %, GM31107+3YSZ10 % glass systems after the corresponding joining thermal treatment at 700 °C. Patterns are normalized to the intensity of the highest peak.

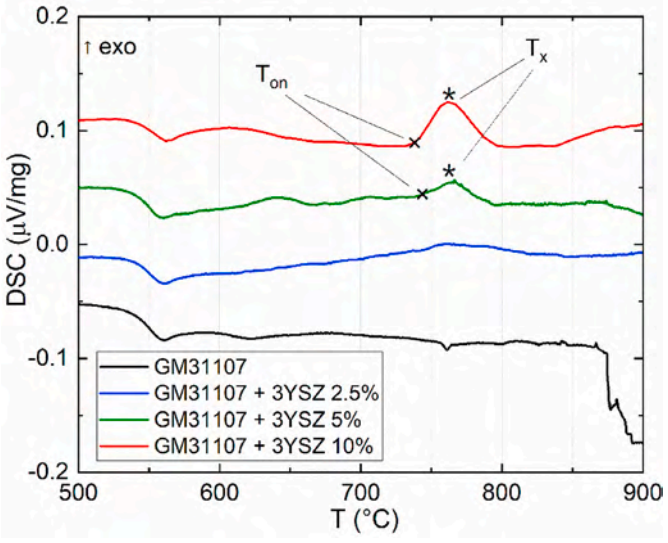

Fig. 4. DSC curves for GM31107, GM31107 + 3YSZ 2.5 %, GM31107 + 3YSZ 5 % and GM31107 + 3YSZ 10 %, glass systems. The crosses (×) indicate the onset of crystallization, while the asterisks (*) mark the crystallization peak temperature for each system.

the reported CTE is ≈ 3×10^{-6} K^{-1} along the *a* and *b* unit cell directions and ≈45×10^{-6} K^{-1} along *c* unit cell direction [50]. No CTE data were found for $Ca_5Ba_2B_{10}O_{22}$ in the literature. Finally, the reported CTE for $CaZrO_3$ is ≈ 10.4×10^{-6} K^{-1} between 0 and 700 °C [51].

Based on the results in Figs. 2–3 and 4, GM31107+3YSZ 5 % was selected as the composite glass-based system for thermo-chemical compatibility testing with AISI 441 and the electrolyte material BZCY622. This system was chosen over GM31107+3YSZ 2.5 % because it exhibits viscous flow behavior and characteristic temperatures of T_g = 548 °C and T_s = 641 °C, which are better aligned with the target PCECs operating temperatures of 500–600 °C. Additionally, the CTE of GM31107+3YSZ 5 % (10.9×10^{-6} K^{-1}) is well matched with that of AISI 441 (12.1×10^{-6} K^{-1} between 20 and 700 °C [24]) and BZCY622

(9.1×10^{-6} K^{-1} between 600 and 900 °C [25]). The presence of the $Ca_5Ba_2B_{10}O_{22}$ crystalline phase does not appear to negatively affect the overall performance of the glass composite. Moreover, the 5 wt% 3YSZ addition does not lead to the formation of Zr-based phases after the joining thermal treatment, unlike the GM31107+3YSZ 10 % system.

3.2. Characterization of the joined samples

Fig. 5 presents the cross-section SEM micrographs of the three different sample configurations assembled in an FSS/glass sealant/half-cell sandwich structure after the corresponding joining thermal treatment. Specifically, Fig. 5a–b, 5c -d, and 5e -f illustrate the AISI441/V11/BZCY622/BZCY622-NiO, AISI441/GM31107/BZCY622/BZCY622-NiO, and AISI441/GM31107+3YSZ 5 %/BZCY622/BZCY622-NiO samples, respectively.

All three configurations show good adhesion and continuity of the glass sealant with both the electrolyte and the interconnector. All three systems, V11, GM31107 and GM31107+3YSZ 5 % are free of cracks and exhibit low closed porosity, ensuring high gas tightness and a hermetic seal.

Fig. 5a–b shows the results of V11, which, as previously reported [22], presents as main crystalline phase Augite ($Ca(Mg_{0.7}Al_{0.3})(S_{1.7}Al_{0.3})O_6$ (#PDF 078–1391). Augite preferentially forms at the AISI441 interface after the joining thermal treatment at 850 °C. At the interface with the electrolyte, various Ba–Mg silicate crystalline phases are observed due to barium diffusion from the BZCY622 into the glass-ceramic matrix. An approximately 3–4 μm thick reaction layer is present in the BCY622 at the interface with V11, indicating substantial interaction between the glass and the electrolyte.

In the GM31107 system (Fig. 5cand d), the glass remains predominantly amorphous after the joining process at 700 °C. No evidence of crystalline phase formation or interdiffusion between the electrolyte and the glass matrix is detected. The interface remains stable and uniform, with no barium depletion from the electrolyte into the glass. This suggests that GM31107 maintains its chemical stability and structural integrity under the joining conditions.

The GM31107 + 3YSZ 5 % system (Fig. 5eand f) exhibits a uniform distribution of 3YSZ (small white granules) within the glass matrix. A homogeneous formation of the crystalline phase $Ca_5Ba_2B_{10}O_{22}$ (darker grey small regions), is also observed, consistent with the XRD results. The presence of 3YSZ does not induce phase separation or degradation of the glass matrix but instead promotes controlled devitrification, leading to the nucleation of Ba- and Ca-rich crystalline phases.

Fig. 6 shows the EDX maps of the glass/electrolyte interface. Fig. 6a, e, and 6i show the selected areas for EDX mapping and point analyses for the AISI441/V11/BZCY622/BZCY622- NiO, AISI441/GM31107/BZCY622/BZCY622-NiO, and AISI441/GM31107+3YSZ 5 %/BZCY622/BZCY622-NiO samples, respectively. The regions for the EDX point analyses are marked with red circles and corresponding numbers, and the results of these analyses are reported in Table 4.

For V11, strong barium diffusion from the electrolyte into the glass-ceramic matrix is evident in the EDX map shown in panel (b). EDX point analyses highlight that the electrolyte splits into two distinct zones: one maintaining the initial composition (point 1) and another (point 2) where the barium percentage significantly decreases, accompanied by the formation of Na- and Ca-silicate phases. The crystalline phases forming at the electrolyte interface have been previously discussed in detail [22].

Referring to the GM31107, the EDX maps shown in panels (f), (g), and (h) illustrate the signals of Ba, Ca, and Al, respectively. No evidence of interdiffusion between the electrolyte and the glass matrix is observed, and the absence of crystalline phase formation after the joining process at 700 °C is confirmed. The interface remains stable and uniform, with no evidence of barium depletion. EDX point analysis confirms that the composition of the glass matches that of the commercial GM31107.

Regarding the composite GM31107+3YSZ 5 %, panel (l) confirms the absence of barium depletion at the electrolyte interface. Similar to the GM31107 sealant, the BZCY622 interface remains stable and uniform. However, panels (m) and (n) showing the distribution of Ca and Al, clearly indicate the formation of a calcium-rich, aluminum-poor crystalline phase, identified by XRD as $Ca_5Ba_2B_{10}O_{22}$. The composition of these crystals is further confirmed by EDX point analysis 1, which shows that in these small dark grey regions, the atomic percentage of calcium is approximately 6 %, compared to 2.5 % in the light grey glass matrix detected at point 3. The small white granules are confirmed by EDX to correspond to the dispersed 3YSZ within the glass matrix. This indicates that the addition of 5 wt% of 3YSZ does not lead to a reaction with the elements of the glass but instead promotes the nucleation of a Ba- and Ca-rich crystalline phases, which grow uniformly within the sealant after the joining thermal treatment at 700 °C.

The EDX maps of the FSS/glass interface for all three systems are

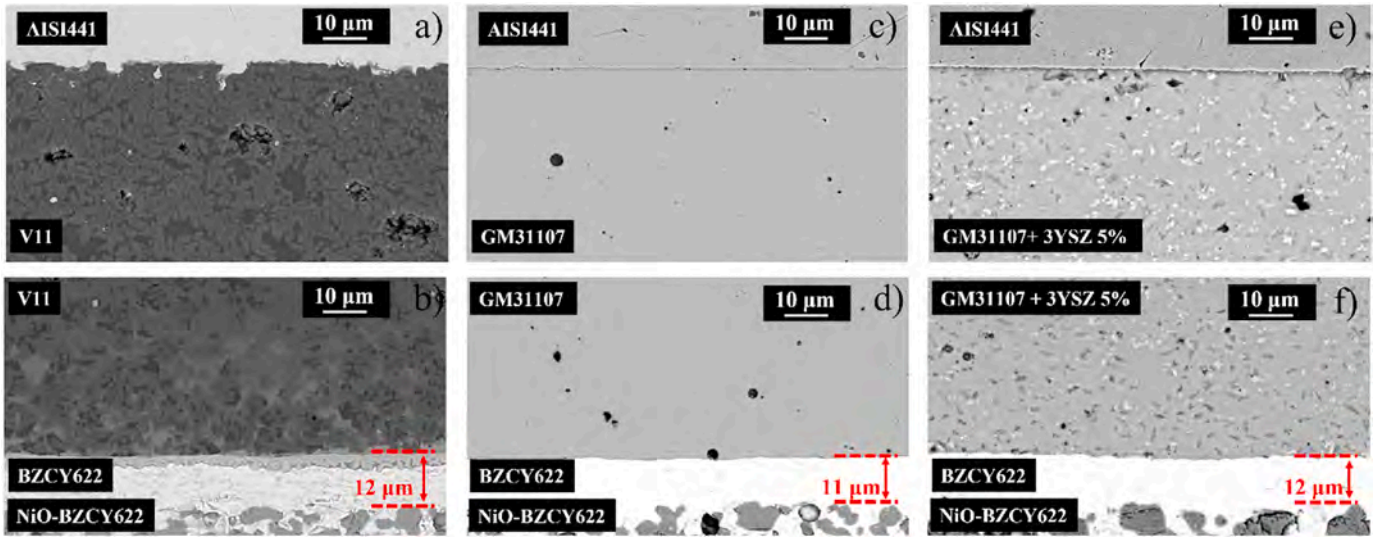

Fig. 5. SEM images of the cross section of three different sample configurations assembled in an FSS/glass sealant/half-cell sandwich structure after the corresponding joining thermal treatment. Panel (a), (c), (e) show the interface between the electrolyte and V11, GM31107 and GM31107+3YSZ 5 %, respectively. Panel (b), (d), (f) show the interface between the AISI441 and V11, GM31107 and GM31107+3YSZ 5 %, respectively. The thickness of the BZCY622 electrolyte in the half-cell is highlighted in red. (For interpretation of the references to color in this figure legend, the reader is referred to the Web version of this article.)

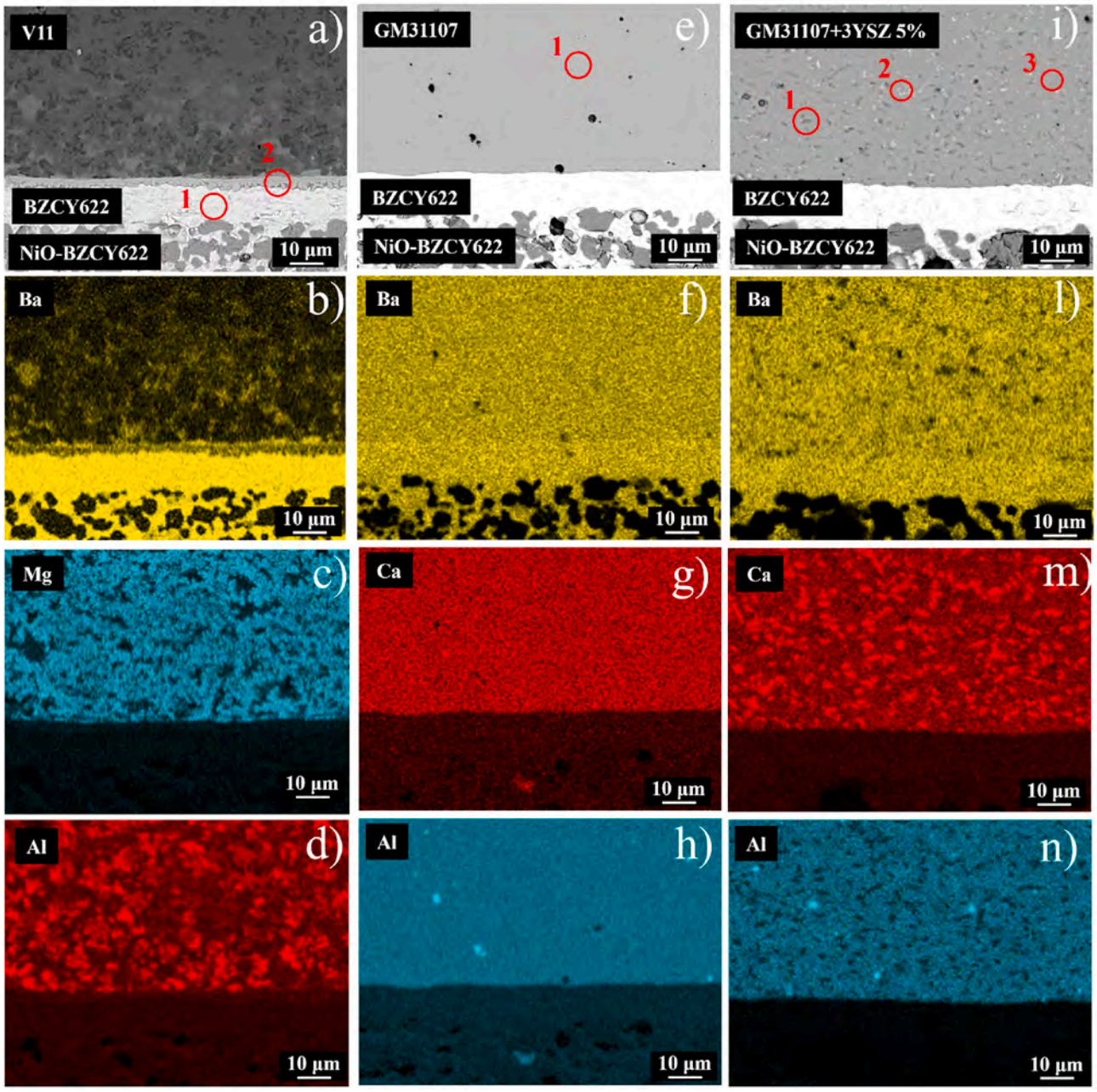

Fig. 6. SEM-EDX analysis of the joined samples after the corresponding joining thermal treatment. Selected areas for the EDX analyses at the interface between the electrolyte and the V11 (a), GM31107 (e) and GM31107+3YSZ 5 % (i). Red circles and corresponding numbers indicate the regions of the EDX point analysis. Ba signal for V11(b), GM31107 (f) and GM31107+3YSZ5 % (l). Mg signal for V11 (c). Ca signal for GM31107 (g) and GM31107+3YSZ 5 % (m). Al signal for V11 (d), GM31107 (h) and GM31107+3YSZ 5 % (n). (For interpretation of the references to color in this figure legend, the reader is referred to the Web version of this article.)

reported in the supplementary materials S1.

The lower joining temperature of 700 °C for the GM31107 and GM31107+3YSZ 5 % systems—compared to the 850 °C required for V11—results in a more stable interface between the electrolyte and the glass, avoiding undesired reactions. GM31107 retains its amorphous structure, whereas GM31107+3YSZ 5 % undergoes controlled devitrification, forming $Ca_5Ba_2B_{10}O_{22}$ as the main crystalline phase without disrupting the integrity of the glass matrix.

3.3. Characterization of the aged samples

Fig. 7 presents the cross-section SEM micrographs of the three different sample configurations assembled in a sandwich structure of FSS/glass sealant/half-cell after the thermal ageing of 500h at 600 °C in an air-steam mixture (70 %–30 % vol.). Specifically, Fig. 7a–b, 7c -d, and 7e -f illustrate the AISI441/V11/BZCY622/BZCY622-NiO, AISI441/GM31107/BZCY622/BZCY622-NiO, and AISI441/GM31107+3YSZ 5 %/BZCY622/BZCY622-NiO samples, respectively.

All three glass systems retain their integrity after thermal ageing, remain free of cracks, and exhibit good adhesion to the electrolyte and FSS interfaces. Fig. 7a–b illustrate that V11 continues to react with the electrolyte. The reaction layer thickness increases from 2 to 3 µm after joining to 5–6 µm following thermal aging. The evolution of crystalline phases in the V11 system after thermal ageing has already been discussed [22].

In the GM31107 system (Fig. 7c and d), darker regions with varying

Table 4
SEM-EDX point analyses performed on the joined samples after the joining thermal treatment in the regions indicated in Fig. 6a, -e and 6i.

At%	GM31107	GM31107+3YSZ 5 %			V11	
	Point 1	Point 1	Point 2	Point 3	Point 1	Point 2
B	23.07	19.5	25.16	23.99	–	–
O	55.25	55.38	57.1	56.14	49.71	54.39
Na	–	–	–	–	–	2.31
Mg	–	–	–	–	–	1.38
Al	7.63	5.1	1.59	6.99	–	1.74
Si	1.15	0.86	0.14	1.06	–	5.67
Ca	2.48	6.08	0.58	2.23	–	3.73
Ni	–	–	–	–	1.06	0.2
Y	–	–	1.12	–	3.61	3.36
Zr	–	0.14	11.14	0.1	15.44	16.31
Ba	10.41	13.39	3.17	9.43	24.89	5.5
Ce	–	–	–	–	5.29	5.41

color contrast and shapes are observed. These features suggest the formation of different crystalline phases during thermal aging, further analyzed using XRD and EDX analyses discussed later. In both GM31107 and GM31107+3YSZ5 %, no large pores are present, implying that significant evaporation of boron species did not occur during thermal ageing. This could be explained by the relatively low vapor pressure of volatile boron species, such as $B(OH)_3$, and the limited mobility of boron-containing species within the glass matrix at 600 °C, which reduces the amount of boron volatilized [40]. This ensures considerable gas tightness. The electrolyte interface remains stable for both systems, with no evidence of interaction with the glass, thus ensuring overall stability even after thermal aging.

To gain further insight into the phase evolution in the boron-based systems, XRD analyses were performed on both GM31107 and GM31107+3YSZ 5 % glass powders after the same thermal aging treatment of 500 h at 600 °C in an air-steam mixture (70 %–30 % vol.). The resulting patterns are presented in Fig. 8.

In the GM31107 system (black curve), the primary phase β-BaB_2O_4 (#PDF 00-024-0086) is observed. This phase, already detected after joining, evolves significantly during thermal aging. In contrast, in the composite GM31107+3YSZ 5 %, the main detected phase is consistently $Ca_5Ba_2B_{10}O_{22}$ (#PDF 00-051-00330), which was already present post-joining and shows no significant evolution.

The EDX maps of the glass/electrolyte interface of the aged samples are presented in Fig. 9. Fig. 9a, e, and 9i show the selected areas for EDX mapping and point analyses for the AISI441/V11/BZCY622/BZCY622-NiO, AISI441/GM31107/BZCY622/BZCY622-NiO, and AISI441/GM31107+3YSZ 5 %/BZCY622/BZCY622-NiO samples, respectively. The areas where the EDX point analyses have been performed are

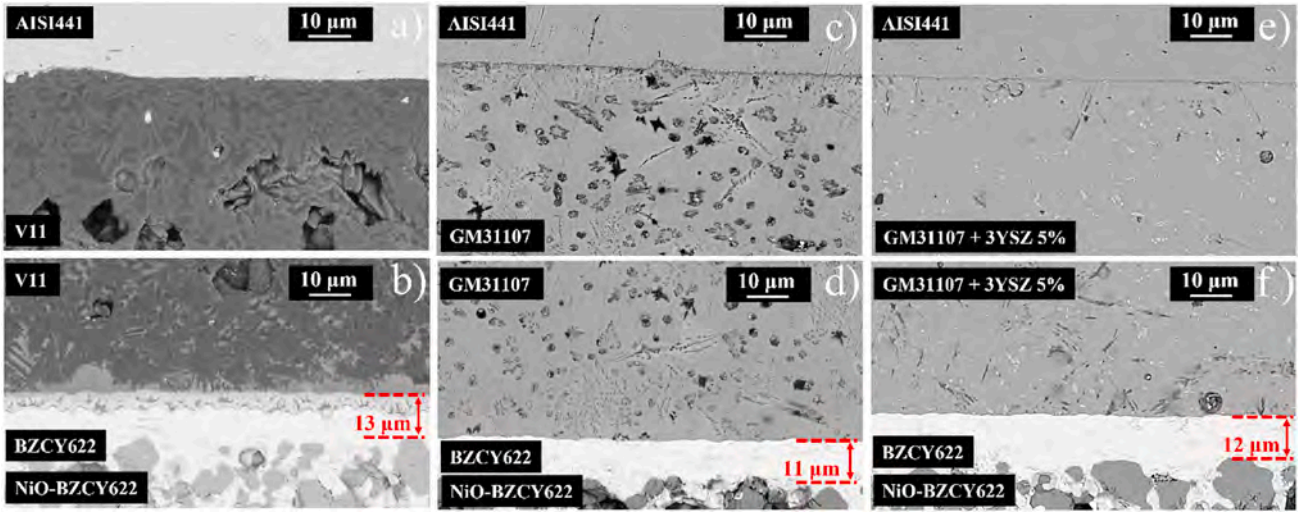

Fig. 7. SEM images of the cross-section of three different sample configurations assembled in a sandwich structure of FSS/glass sealant/half-cell after the thermal ageing of 500h at 600 °C in an air-steam mixture (70 %–30 % vol.). Panel (a), (c), (e) show the interface between the electrolyte and V11, GM31107 and GM31107+3YSZ 5 %, respectively. Panel (b), (d), (f) show the interface between the AISI441 and V11, GM31107 and GM31107+3YSZ 5 %, respectively. The thickness of the BZCY622 electrolyte in the half-cell is highlighted in red. (For interpretation of the references to color in this figure legend, the reader is referred to the Web version of this article.)

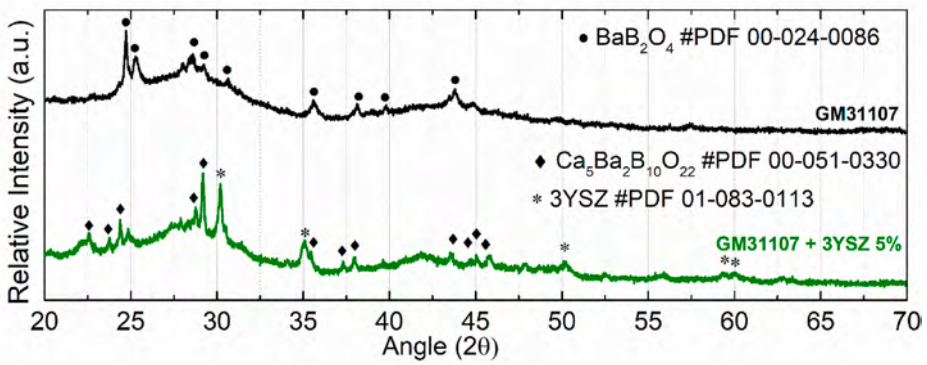

Fig. 8. XRD pattern of the GM31107 and GM31107 + 3YSZ 5 % glass systems after the thermal aging of 500h at 600 °C in air-steam mixture (70 %–30 % vol.). Patterns are normalized to the intensity of the highest peak.

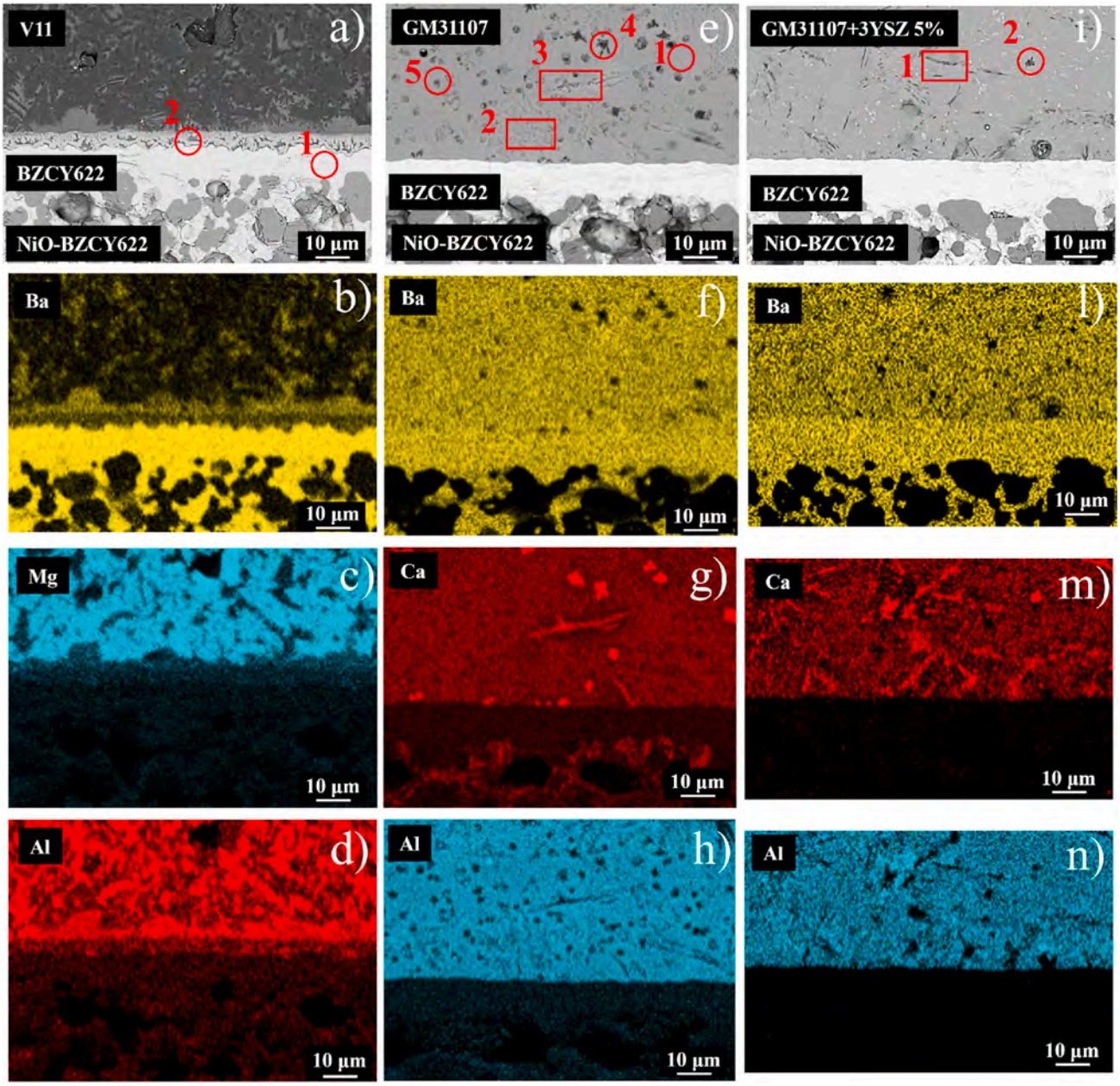

Fig. 9. SEM-EDX analysis of the joined samples after the thermal aging of 500h at 600 °C in air-steam mixture (70 %–30 % vol.). Selected areas for the EDX analyses at the interface between the electrolyte and the V11 (a), GM31107 (e) and GM31107+3YSZ 5 % (i). Red circles and rectangles with the corresponding number indicate the regions of the EDX point analysis. Ba signal for V11(b), GM31107 (f) and GM31107+3YSZ5 % (l). Mg signal for V11 (c). Ca signal for GM31107 (g) and GM31107+3YSZ 5 % (m). Al signal for V11 (d), GM31107 (h) and GM31107+3YSZ 5 % (n). (For interpretation of the references to color in this figure legend, the reader is referred to the Web version of this article.)

marked with red circles, squares, and corresponding numbers. The results of these analyses are reported in Table 5. V11 shows significant Ba depletion in the electrolyte, as in panel (b). EDX point analysis (point 2) confirms a decrease in Ba atomic percentage from 5.5 % after joining to 3.4 % following thermal aging. This confirms the progression of instability at the BZCY622/V11 interface. In contrast, no Ba depletion is observed in the electrolyte after thermal aging for GM31107 and GM31107+3YSZ 5 %, as shown in panels f) and l).

For GM31107, panels (f), (g), and (h), which depict Ba, Ca, and Al signals respectively, reveal the formation of various crystalline phases. The dark grey star-shaped phase (point 4) is rich in Ca but depleted in Ba and Al. EDX point analysis highlights a 17.82 % atomic percentage of Ca, suggesting the formation of a calcium borate phase possibly not detected by XRD. The light grey, long and thin crystalline phase (point 3) is rich in Ca and Ba and poor in Al. EDX point analyses confirm that it corresponds to $Ca_5Ba_2B_{10}O_{22}$, previously identified in GM31107+3YSZ 5 % post-joining. Points 2 and 5 correspond to $BaBO_2$, the main phase detected by XRD. This phase appears in two distinct forms: round-shaped (point 5) and small, dispersed granules (point 2).

For GM31107+3YSZ 5 %, only two crystalline phases are detected after thermal aging, as shown in panels (m) and (n), depicting Ca and Al signals, respectively. The Ca- and Ba-enriched, Al-depleted phase at point 1 corresponds to $Ca_5Ba_2B_{10}O_{22}$, while point 2 marks the star-shaped calcium borate phase, also observed in the GM31107 system.

The EDX maps of the FSS/glass interface for all three systems after the thermal aging are reported in the supplementary materials S2.

These analyses reveal that the BZCY622 electrolyte remains stable at the interface with the GM31107 and GM31107+3YSZ 5 % sealants, even

Table 5
SEM-EDX point analyses were performed on the joined samples after 500 h of thermal aging at 600 °C in an air-steam mixture (70 %–30 % vol.) in the regions indicated in Fig. 9a–e, and 9i.

At%	GM31107					GM31107+3YSZ 5 %		V11	
	Point 1	Point 2	Point 3	Point 4	Point 5	Point 1	Point 2	Point1	Point 2
B	20.67	20.4	19.92	21.63	22.9	16.37	22.45	–	–
O	55.05	53.44	56.47	54.76	52.64	56.17	55.4	55.59	55.63
Na	–	–	–	–	–	–	–	–	2.46
Mg	–	–	–	–	–	–	–	–	1.57
Al	8.6	4.92	4.83	1.99	3.7	4.16	2.16	–	3.1
Si	1.26	1.1	0.98	0.39	1.19	0.71	0.45	–	8.3
Ca	3.02	3.61	6.53	17.82	3.26	6.73	16.94	–	1.52
Ni	–	–	–	–	–	–	–	2.36	0.25
Y	–	–	–	–	–	0.12	–	2.83	2.33
Zr	–	–	–	–	–	1.37	–	13.41	16.46
Ba	11.4	16.53	11.27	3.41	16.31	14.37	2.6	21.44	3.4
Ce	–	–	–	–	–	–	–	4.37	4.98

after thermal aging. In contrast, the electrolyte strongly evolves with V11. However, the GM31107 system undergoes significant evolution and devitrification, in contrast to its fully amorphous state preserved after the joining thermal treatment. The addition of 5 wt% 3YSZ enhances the thermal stability of the boron-based glass. Specifically, it promotes the formation of the crystalline phase $Ca_5Ba_2B_{10}O_{22}$ in the GM31107+3YSZ 5 % composite immediately after joining, which remains stable and does not evolve significantly during the thermal aging. Additionally, 3YSZ inhibits the formation of $BaBO_2$, a phase with a CTE of $3 \times 10^{-6}\ K^{-1}$ along the *a* and *b* unit cell direction and $45 \times 10^{-6}\ K^{-1}$ along the *c* unit cell direction, which significantly affects the thermo-mechanical properties of the sealant. As a result, the CTE of the GM31107 system decreases substantially from $11.4 \times 10^{-6}\ K^{-1}$ post -joining to $10.2 \times 10^{-6}\ K^{-1}$ after thermal ageing. In contrast, the CTE of the GM31107+3YSZ 5 % system decreases only from $10.9 \times 10^{-6}\ K^{-1}$ to $10.6 \times 10^{-6}\ K^{-1}$, demonstrating its superior thermo-mechanical stability.

Another advantage of inducing the growth of a stable borate-containing crystalline phase, as in the GM31107+3YSZ 5 % composite, is that it can reduce boron volatile species formation. A previous study [52] demonstrated how, in a Sr–Ba–borosilicate glass-ceramic, the weight loss of these materials when exposed to wet-forming gas at 780 °C for 28 days decreases by a factor of two as the borate content increases from 10 to 40 mol%. The significant improvement in stability against volatility has been attributed to the formation of SrB_2O_4, which increases with increasing borate content and can fix boron in crystalline phases, thereby reducing its mobility. Similarly, the formation of $Ca_5Ba_2B_{10}O_{22}$ in the GM31107+3YSZ 5 % composite could reduce the volatilization of boron species. This can minimize pore formation and prevent the loss of mechanical properties in the sealant, enhancing its chemical and structural stability [53]. These results are of great importance and demonstrate that the GM31107+3YSZ 5 % system is a promising sealant for long-term applications in PCEC integration.

3.4. Characterization of the thermally cycled samples

Fig. 10 presents the cross-section SEM micrographs of the three different sample configurations assembled in a sandwich structure of FSS/glass sealant/half-cell after the thermal cycling six times from 25 to 600 °C (dwell of 2h) in an air-steam mixture (70 %–30 % vol.). Specifically, Fig. 10a, b, and 10c illustrate the AISI441/V11/BZCY622/BZCY622-NiO, AISI441/GM31107/BZCY622/BZCY622- NiO, and AISI441/GM31107+3YSZ 5 %/BZCY622/BZCY622-NiO samples, respectively.

V11 (Fig. 10a) exhibits two cracks traversing the glass-ceramic, one of which propagates into the cell. In contrast, GM31107 and GM31107+3YSZ 5 % maintain their structural integrity after thermal cycling, remaining free of cracks and showing strong adhesion to both the electrolyte and the FSS interfaces. GM31107 has a thickness of approximately 130 μm, while GM31107+3YSZ 5 % exhibits a reduced thickness of around 60 μm. Both sealants exhibit low closed porosity, with GM31107+3YSZ 5 % being nearly pore-free. All three systems have a CTE compatible with AISI411 and BZCY622 (see section 3.1); however only GM31107 and GM31107+3YSZ 5 % effectively relaxed the stresses induced during thermal cycling due to CTE mismatches and the chemical expansion of the perovskite. At 600 °C, these systems operate just above their glass transition temperature range, enabling self-healing mechanisms to repair potential microcracks. Conversely, V11 remains too rigid at 600 °C to effectively relax stresses.

During operation, PCEC stacks are often subject to both voluntary and involuntary thermal cycling, which can involve minor or significant temperature fluctuations. Therefore, the ability of the boron-based GM31107 glass and GM31107 +3YSZ 5 % glass-composite sealants to remain intact under severe thermal cycling in a steam-rich atmosphere is crucial in demonstrating their suitability as sealants for PCEC applications.

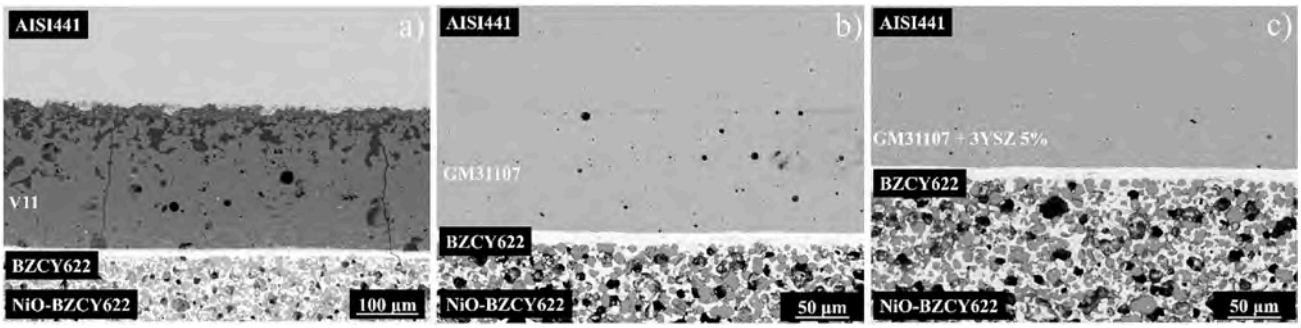

Fig. 10. SEM images of the cross section of three different sample configurations assembled in a sandwich structure of FSS/glass sealant/half-cell after the thermal aging of 500h at 600 °C in an air-steam mixture (70 %–30 % vol.).

4. Conclusions

A commercial boron-based glass and its derived composite, obtained by incorporating 5 wt% 3YSZ, were evaluated as sealants for PCECs applications, and compared to a silica-based glass designed for high-temperature SOECs. The boron-based glass and its composite exhibited lower T_g (500–600 °C) compared to the silica-based glass (600–700 °C), making them suitable for PCECs operation. The composite approach enhanced the sealant's T_s, viscosity, and thermal stability. The incorporation of 3YSZ induced the formation of a Ca–Ba borate crystalline phase, which stabilized the boron in the glass matrix and reduced volatilization of boron rich species in steam-rich environments. Post-aging analysis at 600 °C after 500 h in an air-steam mixture (70 %–30 % vol) revealed superior thermal stability for the composite system, with a more pronounced evolution of the glass structure and devitrification observed in the boron-based glass. Both the boron-based glass and its composite remained crack-free after severe thermal cycling. These results position the boron-based glass, particularly the composite, as a promising sealant for PCEC up-scaling and integration. Future work will focus on modifying the boron-based glass to induce controlled crystalline phases, thereby enhancing thermal stability without the need for external additives.

Funding

This work was supported by SNAM H2 Innovation Center.

CRediT authorship contribution statement

Francesco Da Prato: Writing – review & editing, Writing – original draft, Visualization, Validation, Methodology, Investigation, Formal analysis, Data curation, Conceptualization. **Simone Anelli:** Writing – review & editing, Visualization, Validation, Supervision, Methodology, Investigation, Formal analysis, Data curation, Conceptualization. **Andrea Moranti:** Writing – review & editing, Visualization, Validation, Methodology, Investigation, Formal analysis, Data curation, Conceptualization. **Domenico Ferrero:** Writing – review & editing, Visualization, Validation, Supervision, Methodology, Investigation, Formal analysis, Data curation, Conceptualization. **Massimo Santarelli:** Writing – review & editing, Validation, Supervision, Resources, Project administration, Funding acquisition. **Federico Smeacetto:** Writing – review & editing, Validation, Supervision, Resources, Project administration, Funding acquisition.

Data availability

Data will be made available on request.

Declaration of generative AI and AI-assisted technologies in the writing process

During the preparation of this work the author(s) used ChatGPT in order to smooth and grammatically correct the written text. After using this tool/service, the author(s) reviewed and edited the content as needed and take(s) full responsibility for the content of the publication.

Declaration of competing interest

The authors declare that they have no known competing financial interests or personal relationships that could have appeared to influence the work reported in this paper.

Acknowledgment

The authors acknowledge the collaborations between SNAM H2 Innovation Center and the Politecnico di Torino that made this work possible.

Appendix B. Supplementary data

Supplementary data to this article can be found online at https://doi.org/10.1016/j.ijhydene.2025.05.286.

References

[1] Hassan Q, Viktor P, Al-Musawi T J, Mahmood Ali B, Algburi S, Alzoubi HM, et al. The renewable energy role in the global energy Transformations. Renew Energy Focus 2024;48. https://doi.org/10.1016/j.ref.2024.100545.
[2] Elalfy DA, Gouda E, Kotb MF, Bureš V, Sedhom BE. Comprehensive review of energy storage systems technologies, objectives, challenges, and future trends. Energy Strategy Rev 2024;54. https://doi.org/10.1016/j.esr.2024.101482.
[3] Breyer C, Lopez G, Bogdanov D, Laaksonen P. The role of electricity-based hydrogen in the emerging power-to-X economy. Int J Hydrogen Energy 2024;49:351–9. https://doi.org/10.1016/j.ijhydene.2023.08.170.
[4] Bhandari R, Adhikari N. A comprehensive review on the role of hydrogen in renewable energy systems. Int J Hydrogen Energy 2024;82:923–51. https://doi.org/10.1016/j.ijhydene.2024.08.004.
[5] Risbud M, Kaur G, Dhawale DS, Zhu H, Haque N, Giddey S. Electrolyzer technologies for hydrogen economy. Hydrogen Economy: processes. Supply chain, life cycle analysis and energy transition for sustainability. Elsevier; 2023. p. 459–85. https://doi.org/10.1016/B978-0-323-99514-6.00003-0.
[6] Medvedev D. Trends in research and development of protonic ceramic electrolysis cells. Int J Hydrogen Energy 2019;44:26711–40. https://doi.org/10.1016/j.ijhydene.2019.08.130.
[7] Patel S, Liu F, Ding H, Duan C, Ghamarian I. On proton conduction mechanism for electrolyte materials in solid oxide fuel cells. Int J Hydrogen Energy 2024;72:1236–48. https://doi.org/10.1016/j.ijhydene.2023.11.012.
[8] Ji H Il, Lee JH, Son JW, Yoon KJ, Yang S, Kim BK. Protonic ceramic electrolysis cells for fuel production: a brief review. J Korean Ceram Soc 2020;57:480–94. https://doi.org/10.1007/s43207-020-00059-4.
[9] Kim D, Lee TK, Han S, Jung Y, Lee DG, Choi M, et al. Advances and challenges in developing protonic ceramic cells. Mater Today Energy 2023;36. https://doi.org/10.1016/j.mtener.2023.101365.
[10] Kasyanova AV, Zvonareva IA, Tarasova NA, Bi L, Medvedev DA, Shao Z. Electrolyte materials for protonic ceramic electrochemical cells: main limitations and potential solutions. Materials Reports. Energy (Calg) 2022;2. https://doi.org/10.1016/j.matre.2022.100158.
[11] Rashid NLRM, Samat AA, Jais AA, Somalu MR, Muchtar A, Baharuddin NA, et al. Review on zirconate-cerate-based electrolytes for proton-conducting solid oxide fuel cell. Ceram Int 2019;45:6605–15. https://doi.org/10.1016/j.ceramint.2019.01.045.
[12] Zhang W, Hu YH. Progress in proton-conducting oxides as electrolytes for low-temperature solid oxide fuel cells: from materials to devices. Energy Sci Eng 2021;9:984–1011. https://doi.org/10.1002/ese3.886.
[13] Bello IT, Zhai S, He Q, Cheng C, Dai Y, Chen B, et al. Materials development and prospective for protonic ceramic fuel cells. Int J Energy Res 2022;46:2212–40. https://doi.org/10.1002/er.7371.
[14] Wang Q, Ricote S, Chen M. Oxygen electrodes for protonic ceramic cells. Electrochim Acta 2023;446. https://doi.org/10.1016/j.electacta.2023.142101.
[15] Choi S, Davenport TC, Haile SM. Protonic ceramic electrochemical cells for hydrogen production and electricity generation: exceptional reversibility, stability, and demonstrated faradaic efficiency. Energy Environ Sci 2019;12:206–15. https://doi.org/10.1039/c8ee02865f.
[16] Le LQ, Hernandez CH, Rodriguez MH, Zhu L, Duan C, Ding H, et al. Proton-conducting ceramic fuel cells: scale up and stack integration. J Power Sources 2021;482. https://doi.org/10.1016/j.jpowsour.2020.228868.
[17] Le LQ, Meisel C, Hernandez CH, Huang J, Kim Y, O'Hayre R, et al. Performance degradation in proton-conducting ceramic fuel cell and electrolyzer stacks. J Power Sources 2022;537. https://doi.org/10.1016/j.jpowsour.2022.231356.
[18] Smeacetto F, Salvo M, Ferraris M, Casalegno V, Asinari P, Chrysanthou A. Characterization and performance of glass-ceramic sealant to join metallic interconnects to YSZ and anode-supported-electrolyte in planar SOFCs. J Eur Ceram Soc 2008;28:2521–7. https://doi.org/10.1016/j.jeurceramsoc.2008.03.035.
[19] Zakaria Z, Awang Mat Z, Abu Hassan SH, Boon Kar Y. A review of solid oxide fuel cell component fabrication methods toward lowering temperature. Int J Energy Res 2020;44:594–611. https://doi.org/10.1002/er.4907.
[20] Wang R, Sun Z, Choi JP, Basu SN, Stevenson JW, Tucker MC. Ferritic stainless steel interconnects for protonic ceramic electrochemical cell stacks: oxidation behavior and protective coatings. Int J Hydrogen Energy 2019;44:25297–309. https://doi.org/10.1016/j.ijhydene.2019.08.041.
[21] Gao J, Si X, Yang B, Yuan H, Zheng M, Li C, et al. TiO2 containing glass sealant for protonic ceramic fuel cell applications: microstructure, strength and stability studied in sealing of BaZr0.1Ce0.7Y0.1Yb0.1O3-δ electrolyte to Crofer 22H interconnect. Ceram Int 2024. https://doi.org/10.1016/j.ceramint.2024.10.035.
[22] Anelli S, Baggio A, Ferrero D, Schmider D, Dailly J, Santarelli M, et al. Characterization and testing of glass-ceramic sealants for protonic ceramic electrolysis cells applications. Ceram Int 2024;50:17520–31. https://doi.org/10.1016/j.ceramint.2024.02.240.

[23] Manjunath N, Santhy K, Rajasekaran B. Thermal expansion of Crofer 22 APU steel used for SOFC interconnect using in-situ high temperature X-ray diffraction. Mater Today Proc 2023. https://doi.org/10.1016/j.matpr.2023.03.113.
[24] ATI. ATI 441 HP™ Ferritic Stainless Steel. ATI Materials. https://www.atimaterials.com/Products/Pages/ati-441-hp.aspx; accessed May 7, 2025.
[25] Løken A, Ricote S, Wachowski S. Thermal and chemical expansion in proton ceramic electrolytes and compatible electrodes. Crystals (Basel) 2018;8. https://doi.org/10.3390/cryst8090365.
[26] Smeacetto F, Chrysanthou A, Sabato AG, Javed H, Pierre SD la, Salvo M, et al. Glass-to-metal seals for solid oxide cells at the Politecnico di Torino, an overview. Int J Appl Ceram Technol 2022;19:1017–28. https://doi.org/10.1111/ijac.13949.
[27] Smeacetto F, Salvo M, D'Hérin Bytner FD, Leone P, Ferraris M. New glass and glass-ceramic sealants for planar solid oxide fuel cells. J Eur Ceram Soc 2010;30:933–40. https://doi.org/10.1016/j.jeurceramsoc.2009.09.033.
[28] Smeacetto F, De Miranda A, Chrysanthou A, Bernardo E, Secco M, Bindi M, et al. Novel glass-ceramic composition as sealant for SOFCs. J Am Ceram Soc 2014;97:3835–42. https://doi.org/10.1111/jace.13219.
[29] Fergus JW. Sealants for solid oxide fuel cells. J Power Sources 2005;147:46–57. https://doi.org/10.1016/j.jpowsour.2005.05.002.
[30] Mahapatra MK, Lu K. Glass-based seals for solid oxide fuel and electrolyzer cells - a review. Mater Sci Eng R Rep 2010;67:65–85. https://doi.org/10.1016/j.mser.2009.12.002.
[31] Hiraiwa C, Han D, Kuramitsu A, Kuwabara A, Takeuchi H, Majima M, et al. Chemical expansion and change in lattice constant of Y-doped BaZrO 3 by hydration/dehydration reaction and final heat-treating temperature. J Am Ceram Soc 2013;96:879–84. https://doi.org/10.1111/jace.12172.
[32] Andersson AKE, Selbach SM, Knee CS, Grande T. Chemical expansion due to hydration of proton-conducting perovskite oxide ceramics. J Am Ceram Soc 2014;97:2654–61. https://doi.org/10.1111/jace.12990.
[33] Hudish G, Manerbino A, Coors WG, Ricote S. Chemical expansion in BaZr0.9−xCexY0.1O3−δ (x = 0 and 0.2) upon hydration determined by high-temperature X-ray diffraction. J Am Ceram Soc 2018;101:1298–309. https://doi.org/10.1111/JACE.15275.
[34] Singh K, Walia T. Review on silicate and borosilicate-based glass sealants and their interaction with components of solid oxide fuel cell. Int J Energy Res 2021;45:20559–82. https://doi.org/10.1002/er.7161.
[35] Gao J, Si X, Li M, Zhao W, Li C, Qi J, et al. A novel non-crystallizing Na2O-K2O-TiO2 silicate glass sealant for protonic ceramic fuel cell applications. Ceram Int 2024. https://doi.org/10.1016/j.ceramint.2024.09.342.
[36] Gao J, Si X, Yang B, Li M, Li C, Qi J, et al. Improving the stability of BaZr0.1Ce0.7Y0.1Yb0.1O3-δ/Crofer 22 H glass-sealed joints in humid oxidizing environments with a Mn-Co spinel coating. Ceram Int 2024. https://doi.org/10.1016/j.ceramint.2024.10.342.
[37] Zhang X yi, ming LIX, Xing X dong. Effect of B2O3 content on viscosity and structure of SiO2−MgO−FeO-based slag. Trans Nonferrous Metals Soc China 2022;32:2403–13. https://doi.org/10.1016/S1003-6326(22)65956-9.
[38] Wang X, Kou Z, Wu H, Song Y, Zhao X, Xu S, et al. Improvement of thermal cycle stability of YSZ-glass composite seals for intermediate temperature solid oxide fuel cell. Ceram Int 2023;49:36734–42. https://doi.org/10.1016/j.ceramint.2023.08.359.
[39] Wang X, Li R, Yang J, Gu D, Yan D, Pu J, et al. Effect of YSZ addition on the performance of glass-ceramic seals for intermediate temperature solid oxide fuel cell application. Int J Hydrogen Energy 2018;43:8040–7. https://doi.org/10.1016/j.ijhydene.2018.03.023.
[40] Zhang T, Fahrenholtz WG, Reis ST, Brow RK. Borate volatility from SOFC sealing glasses. J Am Ceram Soc 2008;91:2564–9. https://doi.org/10.1111/j.1551-2916.2008.02479.x.
[41] Ritucci I, Agersted K, Zielke P, Wulff AC, Khajavi P, Smeacetto F, et al. A Ba-free sealing glass with a high coefficient of thermal expansion and excellent interface stability optimized for SOFC/SOEC stack applications. Int J Appl Ceram Technol 2018;15:1011–22. https://doi.org/10.1111/ijac.12853.
[42] Mahapatra MK, Lu K, Bodnar RJ. Network structure and thermal property of a novel high temperature seal glass. Appl Phys A Mater Sci Process 2009;95:493–500. https://doi.org/10.1007/s00339-008-4926-z.
[43] Rao P, Singh RN. Sintering and thermal expansion behaviors of glass and glass–YSZ composites as self-repairable seals for SOFC. J Am Ceram Soc 2023;106:157–65. https://doi.org/10.1111/jace.18534.
[44] Rossler E, Hess K-U, Novikov VN. Universal representation of viscosity in glass forming liquids, 223; 1998.
[45] Chen C, Zeng H, Deng Y, Yan J, Jiang Y, Chen G, et al. A novel viscosity-temperature model of glass-forming liquids by modifying the eyring viscosity equation. Appl. Sci. (Switzerland) 2020;10. https://doi.org/10.3390/app10020428.
[46] Lopes AAS, Soares RS, Lima MMA, Monteiro RCC. Glass transition and crystallization kinetics of a barium borosilicate glass by a non-isothermal method. J Appl Phys 2014;115. https://doi.org/10.1063/1.4863334.
[47] Ren H, Ge W, Chen L, Peng H, Meng F, Lin H, et al. Low thermal stress and excellent gas tightness in BaO−CaO−Al2O3−B2O3−SiO2 glass-ceramic for long-term ITSOFC application. J Am Ceram Soc 2024. https://doi.org/10.1111/jace.20197.
[48] Brochu M, Gauntt BD, Shah R, Miyake G, Loehman RE. Comparison between barium and strontium-glass composites for sealing SOFCs. J Eur Ceram Soc 2006;26:3307–13. https://doi.org/10.1016/j.jeurceramsoc.2005.08.002.
[49] Hayashi H, Saitou T, Maruyama N, Inaba H, Kawamura K, Mori M. Thermal expansion coefficient of yttria stabilized zirconia for various yttria contents. Solid State Ionics 2005;176:613–9. https://doi.org/10.1016/j.ssi.2004.08.021.
[50] Filatov SK, Nikolaeva NV, Bubnova RS, Polyakova IG. Thermal expansion of β-BaB2O4 and BaB 4O7 borates. Glass Phys Chem 2006;32:471–8. https://doi.org/10.1134/S1087659606040110.
[51] Zhu Q, Peng L, Zhang T. Sealants for planar solid oxide fuel cells. Materials for high-temperature fuel cells. wiley; 2012. p. 215–44. https://doi.org/10.1002/9783527644261.ch6.
[52] Zhang T, Zou Q. Tuning the thermal properties of borosilicate glass ceramic seals for solid oxide fuel cells. J Eur Ceram Soc 2012;32:4009–13. https://doi.org/10.1016/j.jeurceramsoc.2012.07.036.
[53] Fang L, Liu H, Zhao D, Yang H, Tang D, Zhang T. Reducing the reaction between boron-containing sealing glass-ceramics and lanthanum-containing cathode: effect of Bi2O3. J Eur Ceram Soc 2014;34:4463–8. https://doi.org/10.1016/j.jeurceramsoc.2014.07.006.